Check for updates

Design and preparation of a new Ni/Arg@zeolite-Y nano-composite: investigation of its performance as a multi-functional and bio-organic catalyst for the one-pot synthesis of thieno[2,3-*d*]pyrimidinones

Mehdi Kalhor, [ID] * Ziba Modares and Vahid Azizkhani [ID] *

This paper describes the design and fabrication of a Ni/Arg@zeolite-Y nanocomposite, and investigates its application as a multifunctional nanocatalyst in the one-pot synthesis of thieno[2,3-*d*]pyrimidinone derivatives. Herein, nickel metal ions were stabilized on NaY zeolite through a sodium exchange process (Ni@zeolite-Y). Then, this catalyst was functionalized *via* the linker 3-chloropropyltriethoxysilane with the basic L-arginine amino acid (Arg@zeolite-NiY). The structure of the nano-catalyst was confirmed using techniques such as FT-IR, XRD, BET, FE-SEM, TGA–DTA, and EDX-MAP. The catalytic activity of this nanocomposite in the green synthesis of thieno-pyrimidines was evaluated. Initially, the feasibility of conducting the reaction with this nano-catalyst was assessed through a one-pot reaction involving the cyclization of 2-amino-4,5,6,7-tetrahydrobenzo[*b*]thiophene-3-carboxamide with various aromatic aldehydes under different conditions. Subsequently, the reaction's generality for synthesizing thienopyrimidines under optimized conditions was successfully demonstrated. Key advantages of this project include the elimination of the toxic homogeneous catalyst hydrochloric acid and the use of green solvent ethanol. Additional benefits are the non-toxic nature, cost-effectiveness, recyclability of the nano-catalyst, ease of product isolation, high yield, and reduced reaction time.

1. Introduction

Nowadays, researchers, using recent advances in nanotechnology and considering the principles of green chemistry, are seeking to design reaction processes that not only minimize negative environmental impacts but also enhance the performance of these processes.[1] This new approach has led to increased attention on the design, synthesis, and application of environmentally friendly nanosized heterogeneous catalysts, facilitating their development.[2,3] In recent decades, the use of heterogeneous nanocatalysts in synthesizing organic compounds has seen significant development due to their unique properties. These features include increased reaction speed and selectivity, a high surface-to-volume ratio, easy separation from the reaction environment, and the ability to be reused.[4–7] One of the intriguing recent advancements in catalysts chemistry is the design and emergence of multi-functional heterogeneous nanocatalysts.[8–11] This category consists of two components: a solid substrate serving as the support and active functional groups fixed onto the solid substrate. Zeolites can be

highlighted as materials acting as supports, possessing exceptional capabilities for multiple surface modifications. Zeolites are meso-porous aluminosilicates minerals commonly used as adsorbents, catalysts, and ion-exchange materials. By modifying them with organic components, their properties can be enhanced for specific applications.[12–14] Organically modified zeolites are a type of zeolite that has been chemically altered to incorporate organic functional groups into their structure.[15–17] The synthetic zeolites are widely employed as heterogeneous catalysts and as ideal supports for homogeneous catalysts, owing to their high surface area, thermal stability, porous crystalline structure, stability in organic solvents, ease of separation from reaction environments, and reusability. These advantageous properties render zeolites invaluable across various industrial and research applications.[12–18]

Amino acids have recently gained significant attention as eco-friendly organocatalysts in organic reactions. Researchers are drawn to amino acids in catalytic reactions due to their distinctive features, such as non-toxicity, safety, dual functionality as catalysts, and their compatibility with various materials. However, their catalytic applications face challenges, including difficulty in separating amino acids from the reaction mixture and their inability to be reused after a single reaction.[19–22] A promising solution to these issues is the immobilization of

Department of Chemistry, Payame Noor University, 19395-4697, Tehran, Iran. E-mail: mekalhor@pnu.ac.ir; mekalhor@gmail.com; vahidazizkhani@pnu.ac.ir; Fax: +98 25 3717 9170; Tel: +98 25 3717 9170

homogeneous organocatalysts onto high-surface-area solid supports, such as polymers, nanosilica and zeolites. Arginine plays a fascinating role in the development of catalysts, especially in increasing catalytic efficiency and stability. Arginine can also be attached to heterogeneous solid supports such as graphitic carbon nitride or magnetic nanoparticles to modify catalyst surfaces, improve their reactivity and selectivity in the synthesis of heterocyclic compounds. In addition, arginine is used in electrocatalysis as a reducing agent and structure guide, and in enzyme catalysis.[23–26]

Heterocyclic compounds can include simple rings like pyridine as well as more complex structures such as purines and pyrimidines. One of the heterocyclic compounds that have shown significant medicinal effects in recent years is thienopyrimidine derivatives, with their biological and therapeutic applications well-documented.[27–31] Thienopyrimidine scaffold is one of the most widely used chemical frameworks in drug development. Due to their structural and isoelectronic resemblance to purines, compounds containing thienopyrimidine have become as a highly appealing element in the creation and development of drug, especially anticancer drugs.[32,33] Research shows that cancer is still the most important health problem with increasing incidence and mortality rates worldwide. Fig. 1 showcases some thienopyrimidine-containing drugs, each exhibiting distinct biological activity profiles.[34]

This underscores the significant efforts dedicated to the synthesis of these heterocycles. Numerous studies have documented the preparation of thieno[2,3-*d*]pyrimidines through a two-step process or a one-pot reaction involving aldehydes and thiophenes substituted with amides and amines, utilizing either conventional methods or diverse catalysts.[35–41] While these methods have significantly advanced the synthesis of these compounds, ongoing efforts to refine and develop these techniques or to establish new synthetic strategies addressing their limitations still remain highly valuable.

Having these facts and in order to continue our ongoing research on the preparation of functionalized nanocatalysts on based zeolites, their performance in chemical reactions and the synthesis of heterocyclic compounds,[42–45] our aim in this paper is to design, prepare, and characterize a hybrid nanosized arginine–nickel catalyst stabilized on a zeolite support (Ni/Arg@zeolite-Y) and evaluate its efficiency in the easy and one-pot synthesis of thienopyrimidinone derivatives (Scheme 1).

2. Experimental

2.1. Apparatus, materials, and measurements

All chemicals were purchased from Merck (Darmstadt, Germany) and Fluka (Buchs, Switzerland), and used without further purification. The progress of the reactions from initiation to completion was monitored using thin-layer chromatography (TLC). The TLC plates used were of the model TLC-grade silica gel-G/UV 254 nm. The Fourier transform infrared spectroscopy (FT-IR) spectra were measured on a Shimadzu IR-470 spectrophotometer equipped with a monitor and a JASCO FT-IR system (KBr disks). Melting points were determined on a Barnstead Electrothermal 9200BZ (UK). ^1H NMR and ^{13}C NMR spectra were recorded on a Varian Unity Inova 500 MHz spectrometer (variable-temperature, 2-channel console with pulsed field gradients). NMR spectra were obtained in DMSO-d_6 solvent and are reported as parts per million (ppm) downfield from tetramethylsilane as internal standard. Mass spectra were taken on a C5975 mass spectrometer (Agilent Technologies). The morphological analysis was performed with a Stereoscan 360-
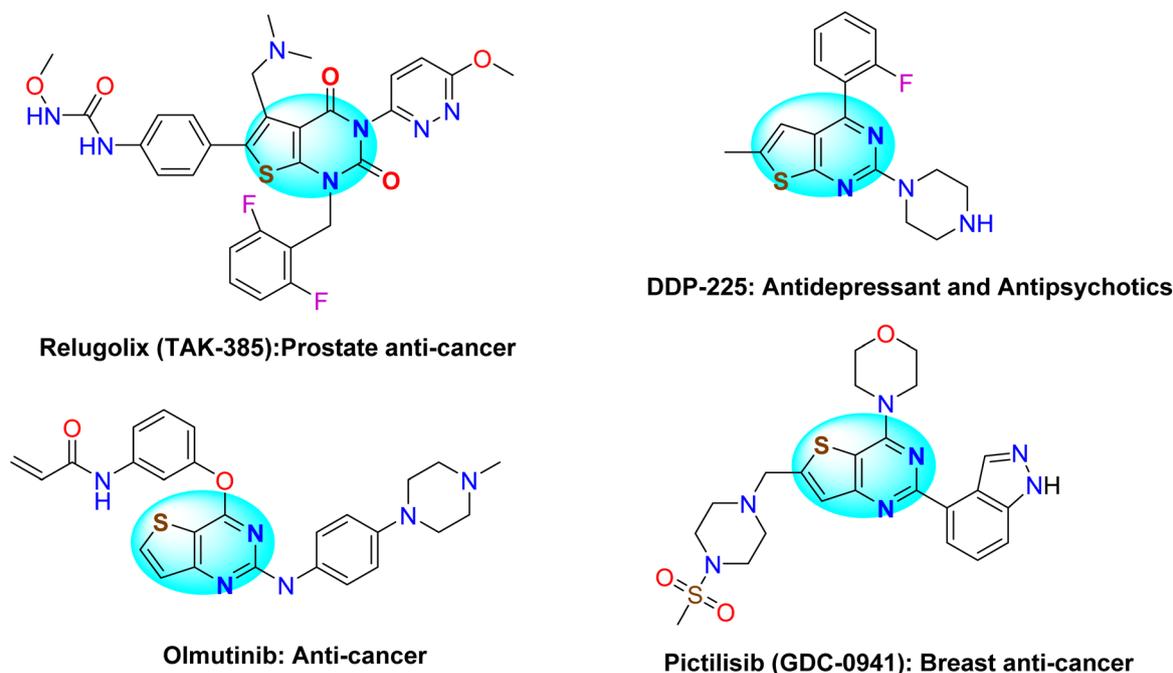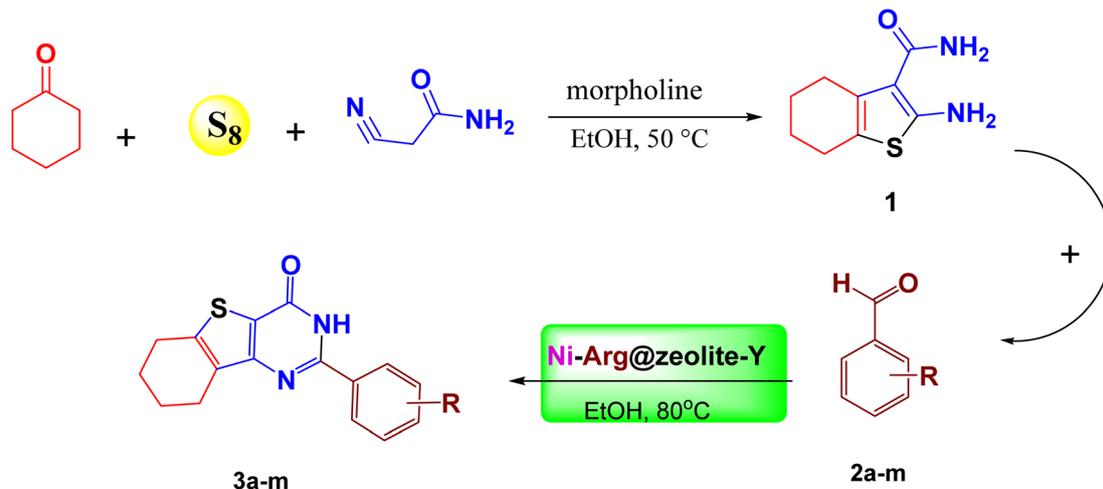

Relugolix (TAK-385): Prostate anti-cancer

DDP-225: Antidepressant and Antipsychotics

Olmutinib: Anti-cancer

Pictilisib (GDC-0941): Breast anti-cancer

Fig. 1 Frameworks of some thienopyrimidine–based drugs.

Scheme 1 The synthetic pathway of thieno[2,3-*d*]pyrimidinones using Ni/Arg@ZY.

Leica/Cambridge Field Emission Scanning Electron Microscope (FE-SEM) that it equipped with energy dispersive X-ray spectrometer (EDX). Nanocomposites based zeolite-Y were characterized using a Holland Philips X'pert X-ray powder diffraction (XRD) diffractometer (CuKα, radiation, $\lambda = 0.154056$ nm), at a scanning speed of $2°$ min^{-1} from $10°$ to $100°$ (2θ). The TGA/DTA measurements were carried out by using a TA-Q600 instrument (made in the USA). TGA/DTA runs were recorded at a scan rate of $10°$ min^{-1} up to 700 °C under pure argon atmosphere. N_2 adsorption and desorption isotherms (BET analysis) of zeolitic samples were measured at the temperature of liquid nitrogen with a Micromeritics system (made in USA). The BET surface area of the nanoparticles was calculated using the Brunauer–Emmett–Teller (BET) method.

2.2. Preparation of Ni/Arg@zeolite-Y nanocomposite

Ni@zeolite-Y nano-structure was prepared according to our previously published method.[43] 1 g of zeolite-NaY is stirred with 1.5 millimoles of nickel chloride at room temperature for 20 hours and then centrifuged. The resulting precipitate is subjected to an ultrasonic bath in three stages, each time washed with water, and then dried at a temperature of 50 to 60 °C. Then, in a 100 mL single-necked round-bottom flask containing toluene (20 mL) and 3-chlorotrimethoxysilane (0.5 mL), 1 g of nano Ni@ZY was added while stirring, and the reaction mixture was refluxed at 111 °C for 24 h. Subsequently, the obtained precipitate, Pr–Cl@zeolite-NiY, was placed in the mixture of water–ethanol and subjected to an ultrasonic bath for 10 minutes in three runs, and then centrifuged. After washing with water, the precipitate was dried in an oven at 50 to 60 °C. In the last step, Pr–Cl@zeolite-NiY (1 g), triethylamine, and arginine (amino acid, 0.025 mmol) were added to a 100 mL round-bottom flask containing 20 mL of toluene. Then, the reaction mixture was refluxed for 24 hours. The obtained precipitate, after three rounds of centrifugation, followed by ultrasonic bath treatment and washing with water, was finally dried at 70 °C.

2.3. General procedure for the synthesis of 3-amino-4,5,6,7-tetrahydrobenzo[*b*]thiophene-2-carboxamide (1)

Compound (**1**) was synthesized in the laboratory following a modified Gewald reaction.[33] A stirred mixture of cyanoacetamide (0.05 mol) and cyclohexanone (0.05 mol) in 10 mL of ethanol at room temperature was combined with sulfur (0.05 mol). Morpholine (5 mL) was then added dropwise, initiating an exothermic reaction. The mixture was stirred at 50 °C for 3 hours before being allowed to stand at room temperature overnight. The resulting yellow solid was collected by filtration, washed with a mixture of ethanol and water, and subsequently dried. Yield: 85%, M. P.: 191 °C, FT-IR (KBr), ν_{max}: 3398–3437 (N–H, amine), 3317–3180 (N–H, amide), 2926 (CH), 1627 (C=O), 1581, 1550 (C=C) cm^{-1}.

2.4. The typical procedure for the catalytic synthesis of thieno[2,3-*d*]pyrimidinones (3a–m)

In a 100 mL single-neck round-bottom flask, a mixture of the synthesized 2-amino-thiophene-3-carboxamide (0.05 g) and the corresponding aromatic aldehydes (1 : 1 molar ratio) in 4 mL of ethanol was combined with 0.0025 g of Arg@zeolite-NiY (3 mol%) and stirred at 80 °C for 10–20 minutes. The progress of the reaction was monitored by thin-layer chromatography (TLC). Upon completion, the catalyst was separated by filtration. Then, a mixture of water and ice was added to the remaining solution to precipitate the product. TLC analysis indicated that the majority of the product was pure. Recrystallization was carried out using a 2 : 8 water/ethanol mixture to further purify the product. Detailed characterization of a number of products, including FT-IR, ^{1}H NMR, and ^{13}C NMR spectra is provided in the SI (Fig. S1–S20).

2.5. Spectroscopic data for select synthesized samples

2.5.1. 2-Phenyl-5,6,7,8-tetrahydrobenzo[4,5]thieno[2,3-*d*] pyrimidin-4(3*H*)-one (3a). FT-IR (KBr, ν_{max}): 3445 (NH), 2923, 2853 (C–H), 1635 (C=O), 1558 (C=N), 1540, 1520, 1507, 1472,
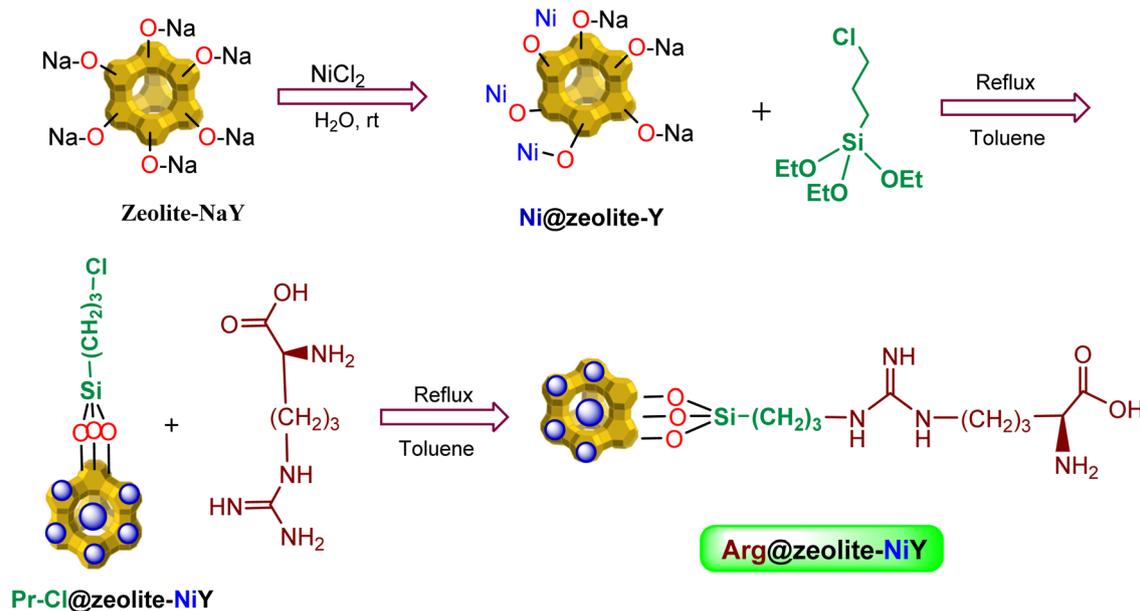
Scheme 2 Synthesis pathway of the Arg@zeolite-NiY nanocatalyst.

1456, 1390, 1339 (C=C), 1019 (C–N), 781 (S–C), 418 cm^{-1}. ^{1}H-NMR (DMSO-d_6, 400 MHz): δ_H 12.50 (s, 1H, NH), 8.14 (d, J = 5.84 Hz, 2H, H-ph), 7.58–7.52 (m, 3H, H-ph), 2.92 (br s, 2H, CH$_2$), 2.77 (br s, 2H, CH$_2$), 1.83–1.80 (br t, 4H, CH$_2$CH$_2$) ppm.

^{13}C-NMR (DMSO-d_6, 100 MHz): δ_C 169.6 (C=O), 154.5, 142.8, 131.3, 128.7, 128.6, 127.8, 127.6, 118.5, 113.4, 25.3, 24.5, 22.5, 21.7 (CH$_2$) ppm.
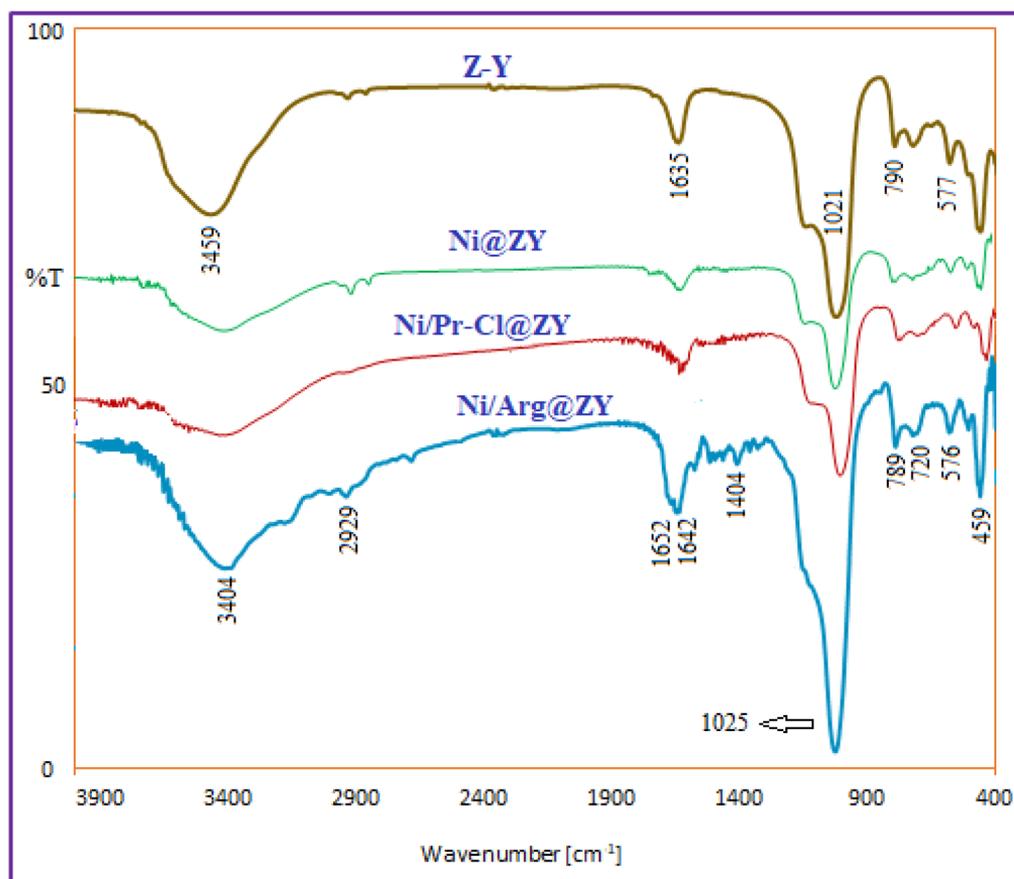

Fig. 2 Comparison of the FT-IR spectra of zeolite-NaY, Ni@ZY, Ni/Pr–Cl@ZY, and Ni/Arg@ZY.

2.5.2. 2-(2-Nitrophenyl)-5,6,7,8-tetrahydrobenzo[4,5]thieno[2,3-*d*]pyrimidin-4(3*H*)-one (3b). FT-IR (KBr, ν_{max}): 3431 (NH), 3082, 2921 (C–H), 1653 (C=O), 1609 (C=N), 1520, 1372 (NO$_2$), 1494, 1301, 1280, 1200 (C=C), 1172, 1012 (C–N), 996, 815 (S–C), 582 cm^{-1}. ^{1}H-NMR (DMSO-d_6, 400 MHz): δ_H 12.87 (br, 1H, NH), 8.20 (d, $J = 7.92$ Hz, 2H, H-Ar), 7.89 (d, $J = 7.40$ Hz, 1H, H-Ar), 7.83 (m, 2H, H-Ar), 2.92 (br s, 2H, CH$_2$), 2.77 (br s, 2H, CH$_2$), 1.81 (br s, 4H, CH$_2$CH$_2$) ppm.

2.5.3. 2-(3-Nitrophenyl)-5,6,7,8-tetrahydrobenzo[4,5]thieno[2,3-*d*]pyrimidin-4(3*H*)-one (3c). FT-IR (KBr, ν_{max}): 3433 (NH), 2937 (C–H), 1650 (C=O), 1590 (C=N), 1485, 1286 (NO$_2$), 1539, 1222 (C=C), 1049, 1010 (C–N), 892 (S–C), 722 cm^{-1}. ^{1}H-NMR (DMSO-d_6, 500 MHz): δ_H 12.73 (br, 1H, NH), 8.94 (s, 1H, H-Ar), 8.55 (d, $J = 7.55$ Hz, 1H, H-Ar), 8.37 (d, $J = 6.75$ Hz, 1H, H-Ar), 7.81 (t, $J = 8.03$ Hz, 2H, H-Ar), 2.91–2.77 (br d, 4H, CH$_2$), 1.82 (br d, 4H, CH$_2$CH$_2$) ppm.
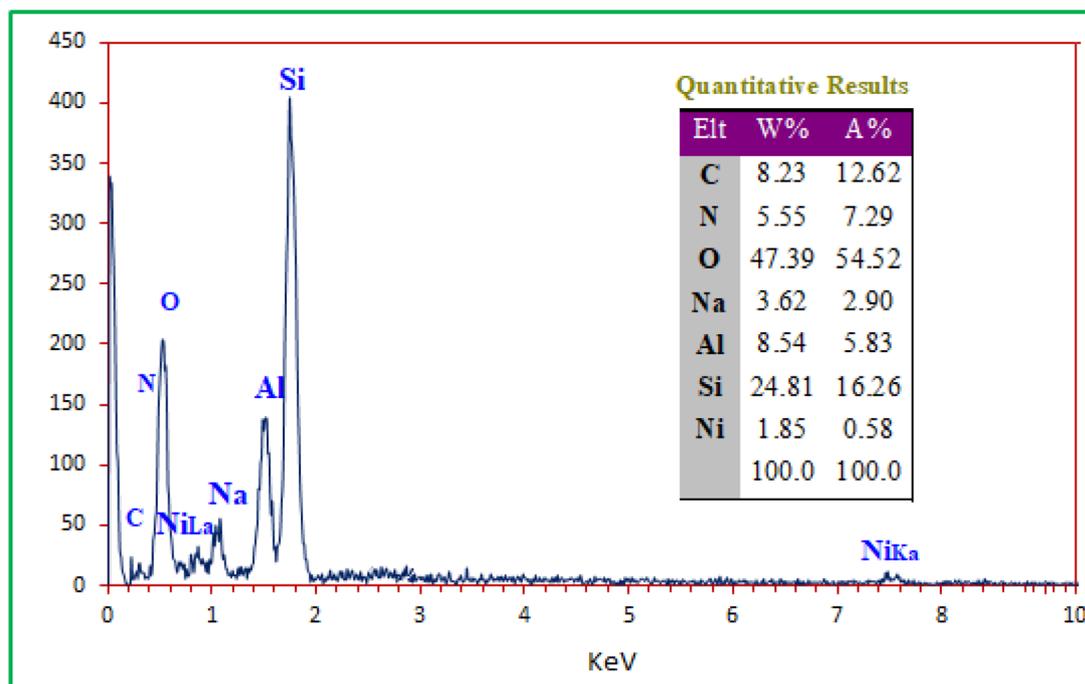

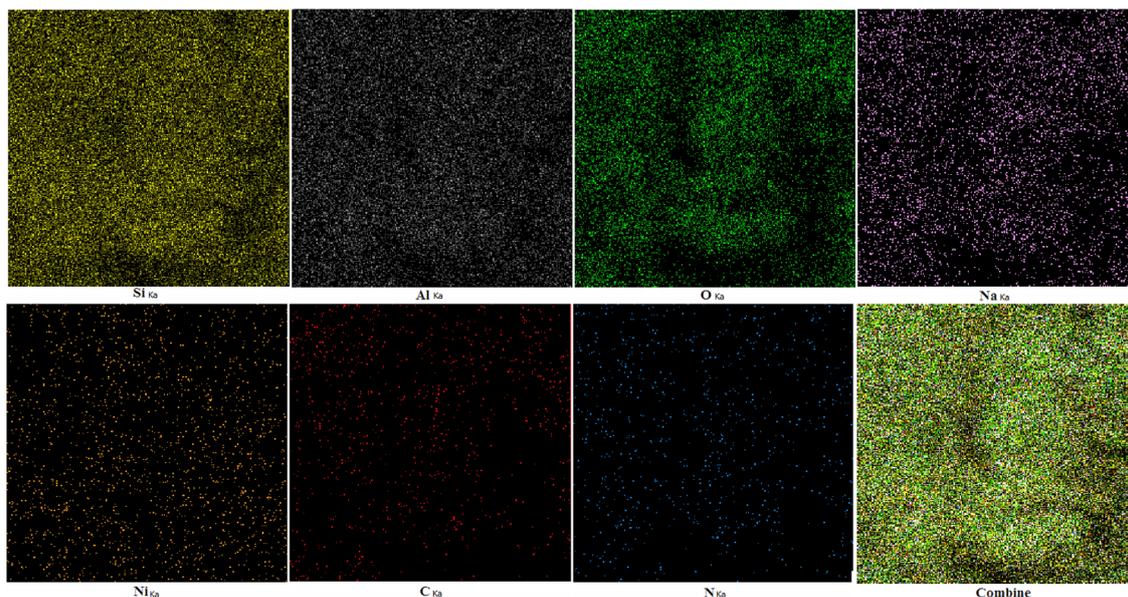**Fig. 3** Energy dispersive X-ray (EDX) analysis of the Ni/Arg@ZY nanocatalyst.

Fig. 4 Elemental distribution map (EDX-MAP) of elements in the Ni/Arg@ZY nanocatalyst.

2.5.4. 2-(4-Nitrophenyl)-5,6,7,8-tetrahydrobenzo[4,5]thieno[2,3-d]pyrimidin-4(3H)-one (3d). FT-IR (KBr, ν_{max}): 3445 (NH), 2926 (C–H), 1651 (C=O), 1530 (C=N), 1519, 1330 (NO$_2$), 1455, 1273 (C=C), 1024 (C–N), 668 (S–C), 419 cm^{-1}. ^{1}H-NMR (DMSO-d_6, 500 MHz): δ_H 12.69 (br, 1H, NH), 8.33 (br d, 4H, H-Ar), 8.55 (d, J = 7.55 Hz, 1H, H-Ar), 8.37 (d, J = 6.75 Hz, 1H, H-Ar), 2.90–2.75 (br d, 4H, 2CH$_2$), 1.81–1.78 (br d, 4H, CH$_2$CH$_2$) ppm.

2.5.5. 2-(4-Bromophenyl)-5,6,7,8-tetrahydrobenzo[4,5]thieno[2,3-d]pyrimidin-4(3H)-one (3e). FT-IR (KBr, ν_{max}): 3432 (NH), 2939 (C–H), 1653 (C=O), 1541 (C=N), 1513, 1416, 1280, 1237 (C=C), 1013 (C–N), 811 (C–Br), 756 (S–C), 418 cm^{-1}. ^{1}H-NMR (DMSO-d_6, 500 MHz): δ_H 12.41 (br, 1H, NH), 8.06 (d, J =

8.00 Hz, 2H, H-Ar), 7.70 (d, J = 6.85 Hz, 2H, H-Ar), 2.91–2.77 (br d, 4H, CH$_2$), 1.82 (br d, 4H, CH$_2$CH$_2$) ppm.

2.5.6. 2-(3-Chlorophenyl)-5,6,7,8-tetrahydrobenzo[4,5]thieno[2,3-d]pyrimidin-4(3H)-one (3f). FT-IR (KBr, ν_{max}): 3444 (NH), 3098, 2930 (C–H), 1648 (C=O), 1532 (C=N), 1340, 1292 (C=C), 1013 (C–N), 788 (C–Cl), 703 (S–C), 418 cm^{-1}. ^{1}H-NMR (DMSO-d_6, 500 MHz): δ_H 12.55 (s, 1H, NH), 8.33 (s, 1H, H-Ar), 8.08 (d, J = 7.70 Hz, 1H, H-Ar), 7.62 (d, J = 8.00 Hz, 1H, H-Ar), 7.55 (t, J = 7.90 Hz, 1H, H-Ar), 2.90 (s, 2H, CH$_2$), 2.75 (s, 2H, CH$_2$), 1.82–1.77 (br d, 4H, CH$_2$CH$_2$) ppm. MS (m/z, %): 316.1 (M$^+$, 100), 288.1 (90), 138.1 (25), 111.1 (20), 91.1 (15).

2.5.7. 2-(3-Methoxyphenyl)-5,6,7,8-tetrahydrobenzo[4,5]thieno[2,3-d]pyrimidin-4(3H)-one (3g). FT-IR (KBr, ν_{max}): 3442
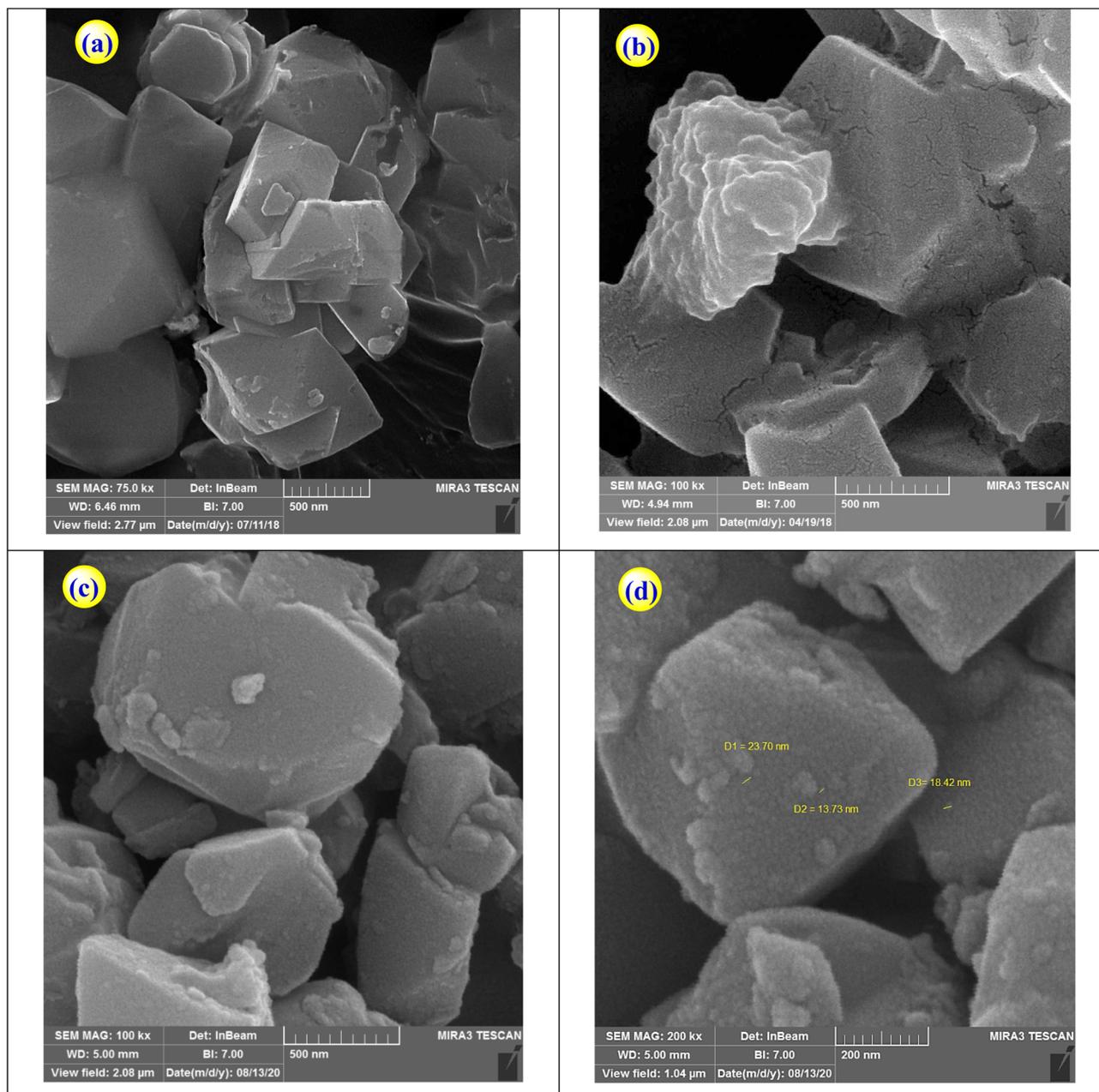

Fig. 5 FE-SEM images of the samples: (a) zeolite-NaY, (b) Ni–ZY, and (c and d) of the Ni/Arg@ZY nanocatalyst.
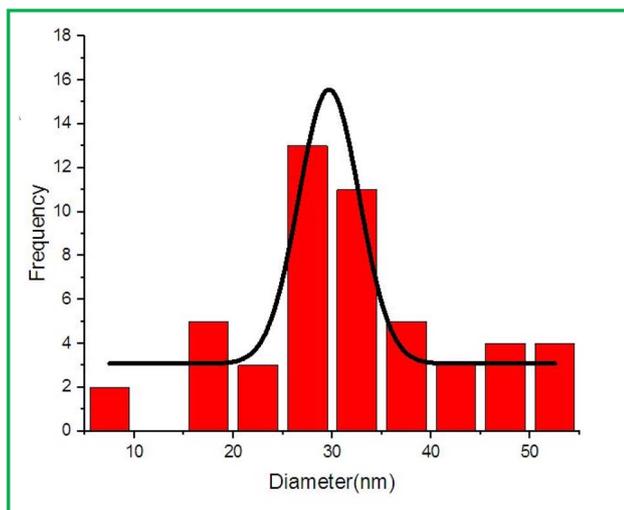
Fig. 6 Histogram of particle size distribution in the Ni/Arg@ZY nanocatalyst.

(NH), 3123, 2932 (C–H), 1654 (C=O), 1592 (C=N), 1545, 1513, 1486, 1327, 1285 (C=C), 1235, 1182 (C–O), 1124, 1007 (C–N), 855 (S–C), 720, 418 cm^{-1}. ^{1}H-NMR (DMSO-d_6, 400 MHz): δ_H 12.51 (s, 1H, NH), 7.73 (d, J = 7.88 Hz, 1H, H-Ar), 7.68 (s, 1H, H-Ar), 7.44 (t, J = 8.01 Hz, 1H, H-Ar), 7.13 (d, J = 8.04 Hz, 1H, H-Ar), 3.85 (s, 3H, OMe), 2.90 (br, 2H, CH$_2$), 2.75 (br, 2H, CH$_2$), 1.80 (br t, 4H, CH$_2$CH$_2$) ppm.

2.5.8. 2-(4-Methoxyphenyl)-5,6,7,8-tetrahydrobenzo[4,5]thieno[2,3-d]pyrimidin-4(3H)-one (3h). FT-IR (KBr, ν_{max}): 3431 (NH), 2930 (C–H), 1654 (C=O), 1538 (C=N), 1448, 1340 (C=C), 1012 (C–N), 714 (S–C) cm^{-1}. ^{1}H-NMR (DMSO-d_6, 500 MHz): δ_H 12.31 (s, 1H, NH), 8.11 (d, J = 8.85 Hz, 2H, H-Ar), 7.05 (d, J = 8.90 Hz, 2H, H-Ar), 3.82 (s, 3H, OMe), 2.88–2.72 (br d, 4H, 2CH$_2$), 1.81–1.75 (m, 4H, CH$_2$CH$_2$) ppm. ^{13}C-NMR (DMSO-d_6, 125 MHz): δ_C 162.2 (C=O), 159.2, 152.2, 132.1, 131.8, 131.2, 129.7, 129.6, 120.7, 114.5, 55.9 (OCH$_3$), 25.8, 24.9, 22.9, 22.2 (CH$_2$) ppm. MS (m/z, %): 312.2 (M$^+$, 100), 284.1 (80), 134.1 (25), 91.1 (20).

2.5.9. 2-(3,4-Dimethoxyphenyl)-5,6,7,8-tetrahydrobenzo[4,5]thieno[2,3-d]pyrimidin-4(3H)-one (3i). FT-IR (KBr, ν_{max}): 3431 (NH), 3093, 2935 (C–H), 1646 (C=O), 1613 (C=N), 1522, 1491, 1486 (C=C), 1295, 1256, 1186 (C–O), 1034 (C–N), 834 (S–C), 594, 403 cm^{-1}. ^{1}H-NMR (DMSO-d_6, 500 MHz): δ_H 12.19 (s, 1H, NH), 7.78–7.72 (m, 2H, H-Ar), 7.07 (d, J = 8.50 Hz, 1H, H-Ar), 3.86 (s, 3H, OMe), 3.83 (s, 3H, OMe), 2.91–2.72 (m, 4H, CH$_2$), 1.81–1.76 (m, 4H, CH$_2$CH$_2$) ppm.

2.5.10. 2-(3,4,5-Trimethoxyphenyl)-5,6,7,8-tetrahydrobenzo[4,5]thieno[2,3-d]pyrimidin-4(3H)-one (3j). FT-IR (KBr, ν_{max}): 3448 (NH), 3079, 2933 (C–H), 1664 (C=O), 1589 (C=N), 1560, 1504, 1432, 1348 (C=C), 1292, 1257, 1197 (C–O), 1090, 1005 (C–N), 964, 781 (S–C), 747, 540 cm^{-1}. ^{1}H-NMR (DMSO-d_6, 400 MHz): δ_H 12.50 (s, 1H, NH), 7.49 (s, 2H, H-Ar), 3.88 (s, 6H, OMe), 3.73 (s, 3H, OMe), 2.91 (br, 2H, CH$_2$), 2.75 (br, 2H, CH$_2$), 1.81 (br t, 4H, CH$_2$CH$_2$) ppm.

2.5.11. 2-(2-Hydroxyphenyl)-5,6,7,8-tetrahydrobenzo[4,5]thieno[2,3-d]pyrimidin-4(3H)-one (3k). FT-IR (KBr, ν_{max}): 3432 (NH), 2939 (C–H), 1653 (C=O), 1541 (C=N), 1513, 1416, 1392, 1289 (C=C), 1261, 1237 (C–O), 1013 (C–N), 811 (S–C), 756, 669, 418 cm^{-1}. ^{1}H-NMR (DMSO-d_6, 500 MHz): δ_H 12.06, 12.00 (br d, 2H, NH and OH), 8.11 (d, J = 7.55 Hz, 1H, H-Ar), 7.41 (t, J = 7.55 Hz, 1H, H-Ar), 7.00–6.94 (m, 2H, H-Ar), 2.88–2.74 (br d, 4H, CH$_2$), 1.80–1.77 (br d, 4H, CH$_2$CH$_2$) ppm.

3. Results and discussion

Given the widespread applications of thienopyrimidines, particularly in the biological and pharmacological fields, the development of effective and efficient methods for the synthesis of these compounds is of significant importance. Therefore, our research team decided to design and synthesize a novel multi-functional nanocatalyst based on arginine and zeolite-Y/Ni to investigate and evaluate its catalytic activity in the synthesis of 2-arylthienopyrimidines under mild conditions. In this section, we will discuss the details of the synthesis and characterization of the nanocatalyst, as well as the synthesis method for 2-arylthienopyrimidines.

3.1. Characterization of the catalyst

Initially, to provide a clearer presentation, the synthesis pathway of Arg@zeolite-NiY is depicted in Scheme 2. First, the Ni@ZY was modified with 3-chloropropyltriethoxysilane to produce Pr–Cl@zeolite-NiY nanocomposites. The zeolite supported L-Arg was then prepared by the reaction of L-arginine amino acid and Ni/Pr–Cl@ZY.

Each component enhances the efficiency of the catalyst, making the multi-functional nanocatalyst more effective when Arg is combined with Ni@ZY, compared to the individual components. Since analyzing the composition, structure, and morphology of nanocatalysts is crucial for predicting their catalytic behavior, the structure of the Ni/L-Arg@ZY catalyst was initially confirmed using various analytical methods.

Table 1 Porosimetry data from BET analysis for zeolite-NaY, Ni@ZY, and Ni/Arg@ZY

Samples	S_{BET}^a (m^2 g^{-1})	V_{BJH}^b (cm^3 g^{-1})	V_{Max}^c (cm^3 g^{-1})	D_{Aap}^d (nm)	W_{BJH}^e (nm)	P_{APS}^f (nm)
Zeolite-NaY	441.3	0.032	0.228	2.213	6.73	13.60
Ni@ZY	269.5	0.019	0.117	2.219	9.34	21.51
Ni/Arg@ZY	300.3	0.021	0.155	2.215	8.03	19.98

^{a} Specific surface area. ^{b} Pore volume. ^{c} Maximum pore volume at P/P_0 = 0.174699824 (estimated using the Horvath–Kawazoe method). ^{d} Adsorption average pore diameter (4V/A by BET). ^{e} BJH adsorption average pore width (4V/A). ^{f} Average nanoparticle size (estimated using the Temkin method).

3.1.1. FT-IR spectroscopic analysis for the Arg@zeolite-NiY nanocatalyst. The FT-IR spectra for zeolite-NaY, Ni@ZY, Ni/Pr–Cl@ZY, and Ni/Arg@ZY are shown in Fig. 2. In the FT-IR spectrum of zeolite-NaY, the broad peaks in the range of 3200–3600 cm^{-1} are attributed to the stretching vibration of the hydroxyl group of water molecules present in zeolite-NaY, while the peak in the range of 1640–1620 cm^{-1} corresponds to its bending vibration. Furthermore, the strong and weak prominent and weak peaks in the regions 1021 cm^{-1} and 790 cm^{-1} correspond to the symmetric and asymmetric stretching vibrations of Si–O–Si groups, respectively. Additionally, the peak in the 470 cm^{-1} region is attributed to the bending vibrations of Si–O–Si or Al–O–Si groups. In FT-IR spectroscopy, metal cation vibrations typically appear in the region of 50–1200 cm^{-1}. The wavelength of these vibrational peaks depends on the nature of the cation and its position. Therefore, it is expected that in the mid-region of the spectrum, *i.e.*, in the range of 400–1400 cm^{-1}, no significant difference will be observed between the FT-IR spectra of zeolite-NaY and Ni@ZY samples. However, since in this region the soft metal nickel replaces the hard metal sodium, it is expected that the peaks will shift slightly towards lower vibrational energy (weaker field) or, in some cases, towards a stronger field. These shifts can be observed in the FT-IR spectrum of the nickel zeolite catalyst. In the FT-IR spectrum of Ni/Pr–Cl@ZY, no significant difference was observed, as only the 3-chloropropyl aliphatic group has been added to the structure. However, the spectrum indicates that the nano-composite structure has been relatively preserved. In the final stage FT-IR spectrum (Fig. 2) corresponding to Ni/Arg@ZY, weak peaks appear in the 1400 to 3200 cm^{-1} regions, which
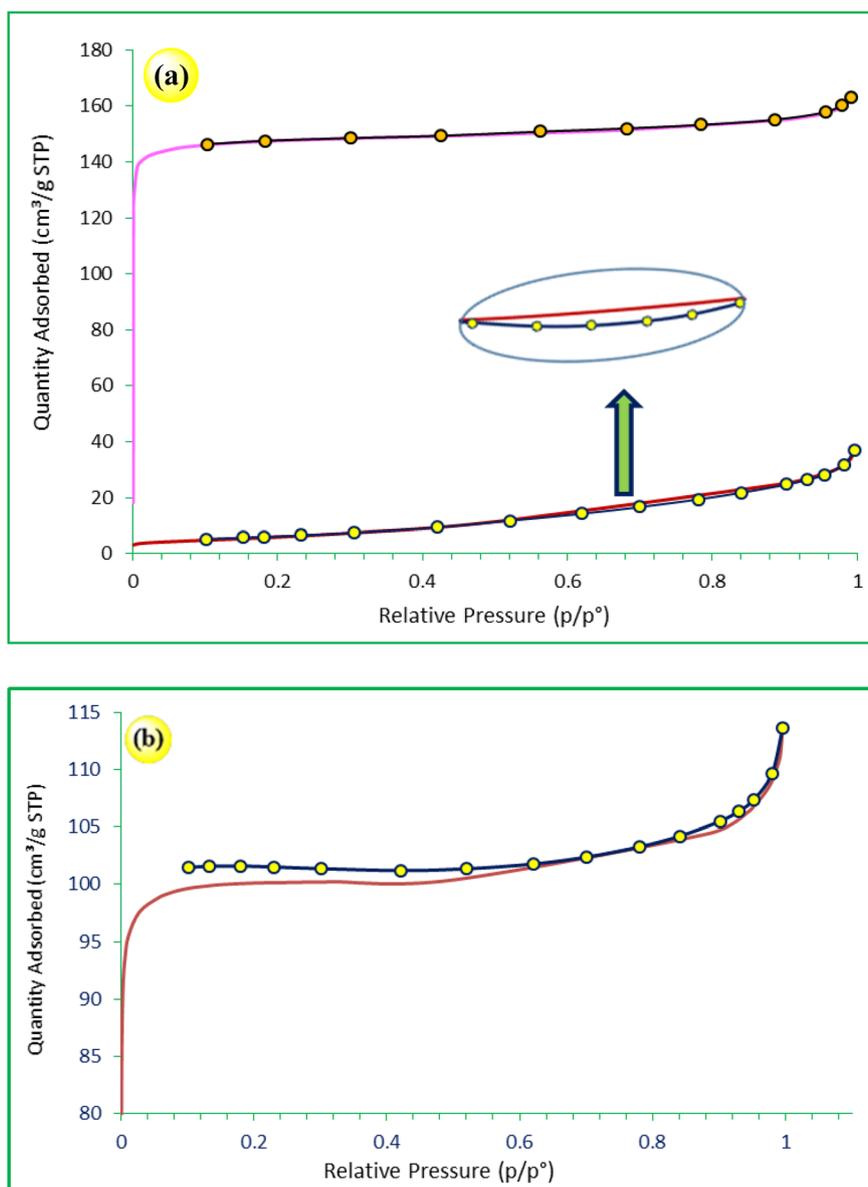

Fig. 7 Adsorption–desorption isotherm curves for samples (a) zeolite NaY, Ni@ZY, and (b) Ni/Arg@ZY.

© 2025 The Author(s). Published by the Royal Society of Chemistry
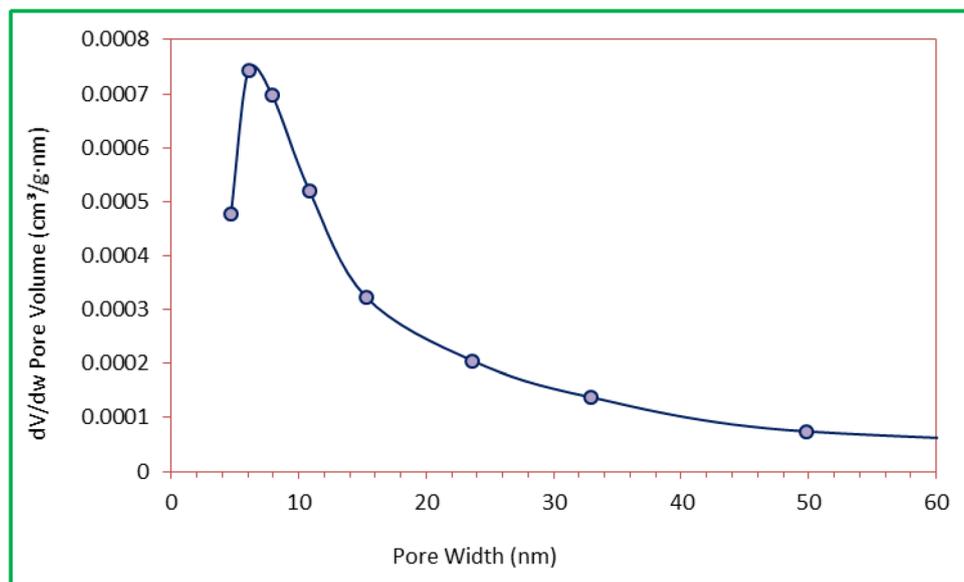
Fig. 8 Pore size distribution chart of the Ni−Arg@ZY nanocatalyst.

are likely attributed to the vibrations of functional groups present in the arginine amino acid (NH, C=N, COOH). Since the amount of arginine immobilized on the nanoporous zeolite support is low, these peaks appear as weak signals. Overall, comparison of the step-by-step FT-IR spectra related to the synthesis of Ni/L-Arg@ZY in Fig. 2 demonstrates the preservation of the crystalline structure.[46,47]

3.1.2. Energy dispersive X-ray (EDX) analysis of the Ni/Arg@ZY nanocatalyst. Energy dispersive X-ray (EDX)

spectroscopy is employed for structural analysis and the elemental composition of the sample. The EDX image of the catalyst nanoparticles is shown in Fig. 3. This image demonstrates that the synthesized nanoparticles are free of impurities and contain the elements C, N, O, Na, Al, Si, and Ni. Additionally, the relative and semi-quantitative atomic and weight percentages of the elements are presented in the table shown in Fig. 3. In this table, the calculated silicon-to-aluminum ratio (Si/Al = 2.90) compared to the initial zeolite (Si/Al = 2.72) confirms
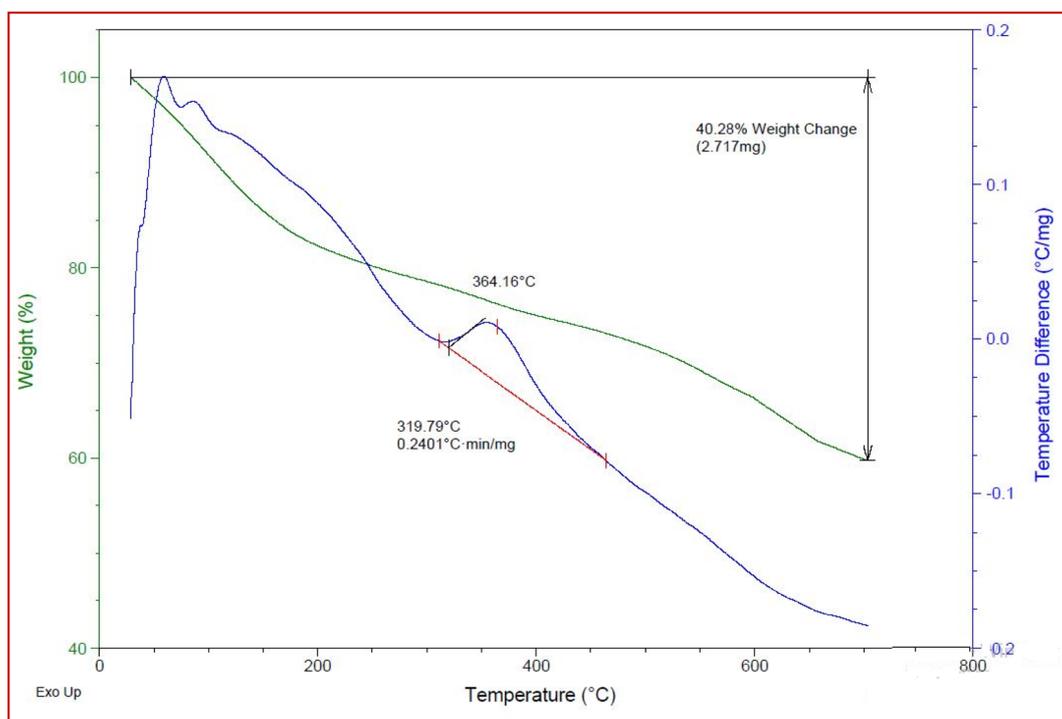

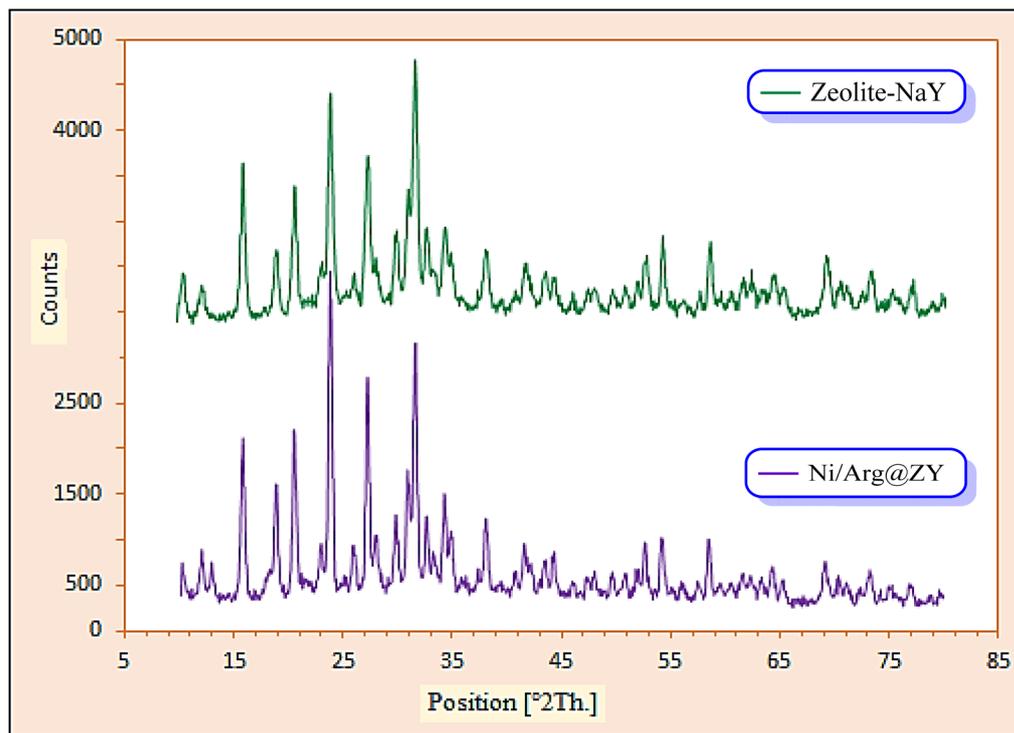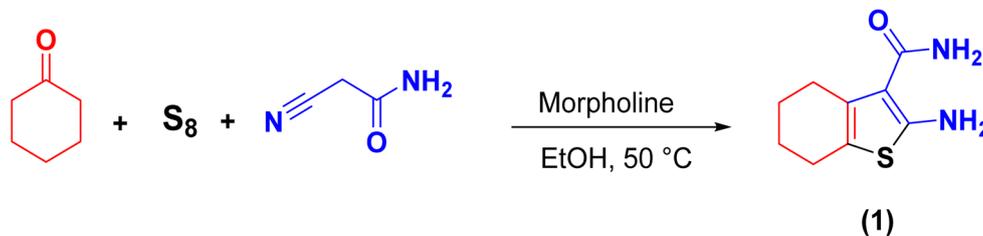Fig. 9 Thermal stability curve (TGA−DTA) of the Ni−Arg@ZY nanocatalyst.

Fig. 10 XRD spectrum of Ni–Arg@ZY nanocatalyst.

Scheme 3 Synthesis route for the preparation of 2-amino-4,5,6,7-tetrahydrobenzo[*b*]thiophene-3-carboxamide (**1**).

the preservation of the Y-type zeolite structure and the relative stabilization and attachment of organo-metallic functional groups on the zeolite support surface. Furthermore, the increase in this ratio indicates the attachment of 3-chloropropyltriethoxysilane to the surface.

Another analysis performed for these nanoparticles, along with the EDX analysis, is the EDX-MAP analysis, as shown in Fig. 4. These images display the spatial distribution of the elements present in the nanocatalyst structure. As observed in the figure, there is a good correlation between the elemental distribution images of the nanoporous structure and the EDX spectrum.

3.1.3. Field emission scanning electron microscopy (FE-SEM) analysis of the Ni/Arg@ZY nanocatalyst. The Field Emission Scanning Electron Microscopy (FE-SEM) images of zeolite-NaY (a), nickel-zeolite (b), and the Ni/Arg@ZY nanocatalyst (c and d) are shown in Fig. 5. These images reveal that the catalyst consists of sheet-like particles with polyhedral pores in small, medium, and large sizes. Furthermore, morphological analysis

of the samples shows that during the functionalization of the initial zeolite, no significant changes occurred in the overall structure of the original zeolite, and its morphology was largely preserved. These images approximate the nanopore sizes to be in the range of 13–23 nm, confirming the desired mesoporous crystalline and nanostructured nature.

Furthermore, based on the statistical distribution chart of particle size or pore diameter on the nanocatalyst support surface obtained from the Field Emission Scanning Electron Microscopy (FE-SEM) image, it was found that most of the particles are in the range of 25–35 nm, and the majority of the pores are in the range of 4–50 nm, which is characteristic of mesoporous materials (Fig. 6).

3.1.4. Brunauer–Emmett–Teller (BET) analysis of the Ni/Arg@ZY nanocatalyst. The results of the pore analysis for the samples of the initial nanozeolite (zeolite-NaY), nickel cation-containing nanozeolite, and the amino-functionalized nickel ion-doped zeolite composite (Ni/Arg@ZY) are presented in

Table 2 Optimizing the reaction conditions for synthesis of 2-phenyl-5,6,7,8-tetrahydrobenzo[4,5]thieno[2,3-*d*]pyrimidin-4(3*H*)-one using Ni–Arg@ZY nanocatalyst[a]
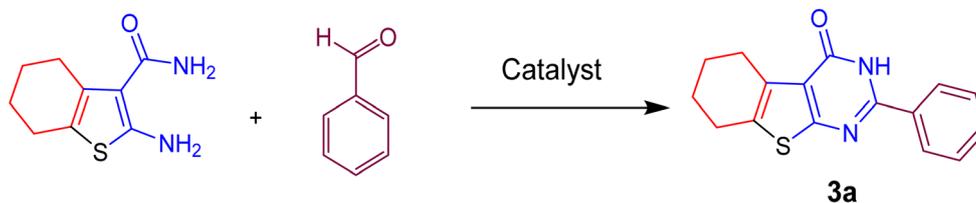
Entry	Catalyst loading (g), (wt/wt%)	Solvent	Temperature (°C)	Time (min)	Yield[b] (%)
1	—	Ethanol	80	24 h	—
2	6	Ethanol	25	300	25
3	6	Ethanol	50	65	60
4	**6**	**Ethanol**	**80**	**15**	**90**
5	3	Ethanol	80	15	55
6	10	Ethanol	80	12	90
7	6	H$_2$O/EtOH (1 : 1 ratio)	80	15	42
8	6	H$_2$O/EtOH (1 : 2 ratio)	80	15	23
9	6	Water	80	30	10
10	6	Methanol	80	65	47
11	6	Acetonitrile	80	240	20
12	6	Ethyl acetate	80	300	15
13	6	—	80	15	35
14	Zeolite-NaY (6 mg)	Ethanol	80	15	—
15	Arg (6 mg)	Ethanol	80	15	20
16	Ni@ZY (6 mg)	Ethanol	80	15	25
17	Ni(NO$_3$)$_2$ (6 mg)	Ethanol	80	15	25

[a] Reaction condition: 2-amino-4,5,6,7-tetrahydrobenzo[*b*]thiophene-3-carboxamide (**1**, 1 mmol), benzaldehyde (1 mmol). [b] Isolated yield.

Table 1. These results indicate that all the samples are mesoporous.

According to the data in Table 1, the specific surface area of the nanocatalyst is approximately 300.3 m^2 g^{-1}, the average pore diameter of the particles is around 2.215 nm, and the average pore width is 8.03 nm. The decrease in the specific surface area of the functionalized catalyst compared to the initial zeolite is likely due to the filling of some of the zeolite pores by the organofunctional groups. This observation (lower desorption) can be seen in Fig. 6.

Fig. 7(a and b) presents the plot of nitrogen gas adsorption and desorption volumes for the various samples synthesized at a constant temperature, providing further confirmation of the successful synthesis of the desired nanomaterials. This curve for zeolite follows the type I isotherm pattern, which is characteristic of porous materials with internal pore diameters smaller than 2 nm. In contrast, the nanocatalysts Ni@zeolite-Y and the multifunctional zeolite composite (Ni/Arg@ZY) follow the type IV isotherm pattern, which exhibits a small hysteresis loop. According to IUPAC classification, the H1 value of these materials lies in the range of $0.78 \leq P/P_0 \leq 0.98$. The presence of a hysteresis loop in the isotherm curve indicates the existence of mesopores with dimensions ranging from 2 to 50 nm in the material's structure. By comparing these hysteresis loops with reference loops, the internal pore geometry can be deduced. The comparison of the hysteresis loop observed in the isotherm

curve of the zeolitic nanostructure clearly indicates the formation of a layered zeolite structure with abundant pores.[48] Additionally, Fig. 8 depicts the pore size distribution chart.

This chart (Fig. 8) shows that most of the pores fall within the range of 4 to 32 nm, which reveals that the overall structure of the nanocomposite contains three types of pores: small, medium, and large. These dimensions are characteristic of mesoporous materials.

3.1.5. TGA–DTA analysis of the Ni/Arg@ZY nanocatalyst. The thermal stability of the catalyst was studied using TGA and DTA thermal analysis (Fig. 9). As shown in Fig. 8, the first weight loss (10.8%, 0.73 mg) occurs in the temperature range of 30–125 °C, which corresponds to the loss of residual solvent and surface water on the sample. The second weight loss (15.3%, 1.03 mg) in the temperature range of 150–440 °C is attributed to the loss of organic groups on the surface of the zeolite. Based on this, it can be concluded that the sample surface is functionalized with organic groups. The third weight loss in the temperature range of 450–650 °C is associated with the structural change of the zeolite and the removal of nickel metal. The total weight loss is approximately 40% of the sample's mass. In the DTA curve, two noticeable decreases are observed, which could correspond to the removal of adsorbed water and water present in the nanozeolite structure. The second peak in the DTA curve may correspond to the removal of organic groups.

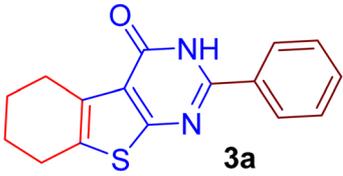**Table 3** Synthesis of thieno[2,3-*d*]pyrimidinone derivatives (**3a–m**) catalyzed by Ni–Arg@ZY[a]
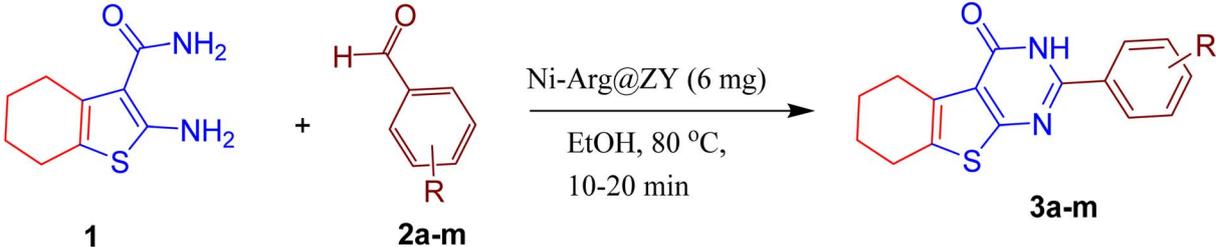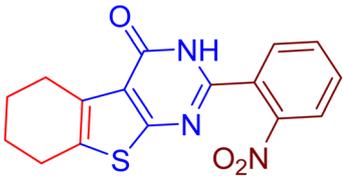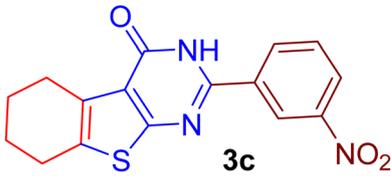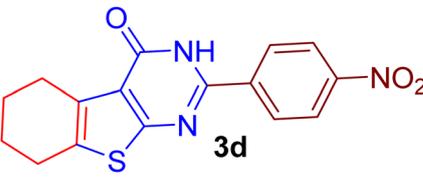

Entry	R₁	Product	M. P. (°C), (lit.)	Time (min)	Yield[b] (%)
1	Ph	**3a**	265–266 (265–268)[31]	15	90
2	2-NO₂	**3b**	299–300	12	92
3	3-NO₂	**3c**	290–292 (290)[33]	14	87
4	4-NO₂	**3d**	298–300 (292)[33]	10	94
5	4-Br	**3e**	328–330 (329–331)[33]	16	88
6	3-Cl	**3f**	298–300	13	89
7	3-OMe	**3g**	289–290 (290)[33]	17	85
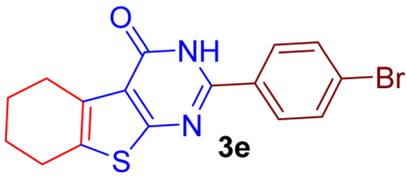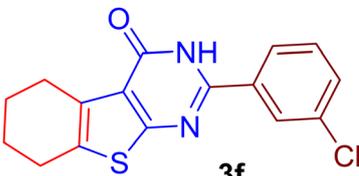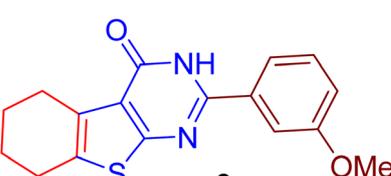
Table 3 (*Contd.*)
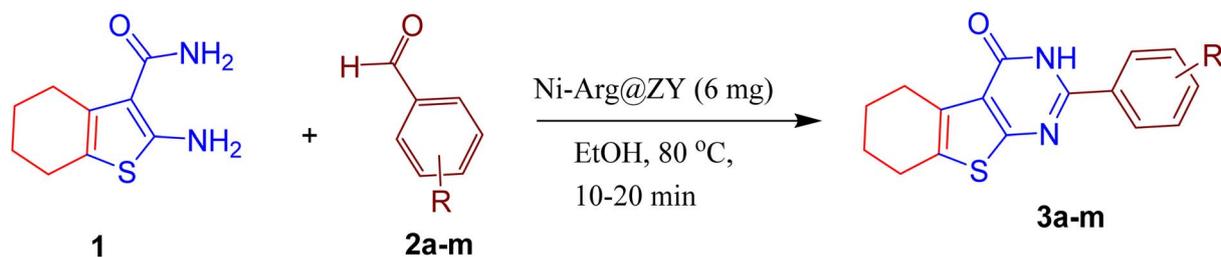
Entry	R_1	Product	M. P. (°C), (lit.)	Time (min)	Yield[b] (%)
8	4-OMe	**3h**	267–268 (269–272)[31]	14	88
9	3,4-OMe	**3i**	280 (281)[33]	13	87
10	3,4,5-OMe	**3j**	296–298 (273–275)[41]	11	86
11	2-OH	**3k**	310–312 (311–314)[31]	17	88
12	4-CH$_3$	**3l**	275–276 (272–274)[35]	20	86
13	4-N(CH$_3$)$_2$	**3m**	228–230 (229–231)[35]	16	85

[a] Reaction condition: 2-amino-4,5,6,7-tetrahydrobenzo[*b*]thiophene-3-carboxamide (**1**, 1 mmol) and aromatic aldehydes (**2a–m**, 1 mmol), Ni–Arg@ZY (6 mg), EtOH as a solvent, under reflux conditions for 10–20 min. [b] Isolated yield.
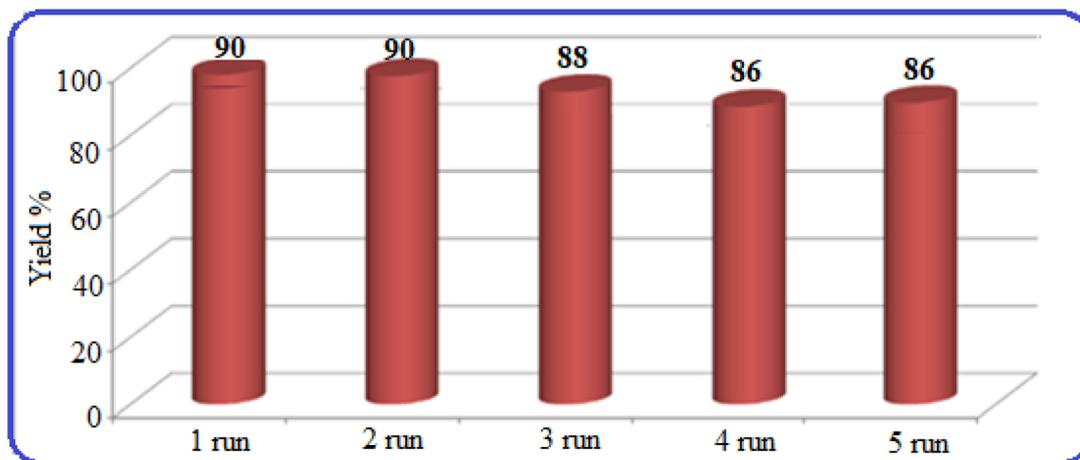
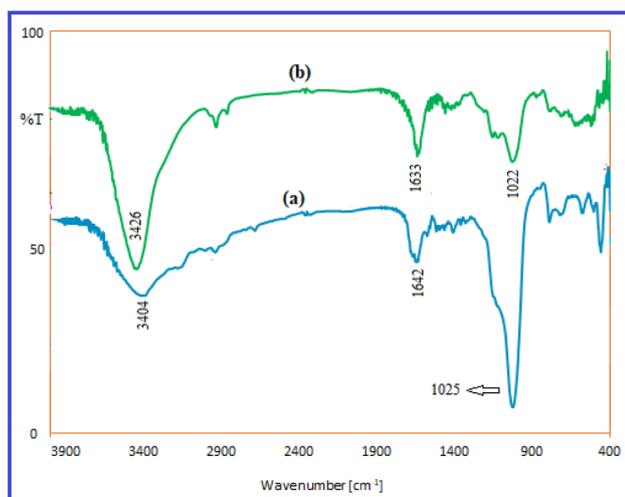**Fig. 11** Reusability of Ni−Arg@ZY nanocatalyst for the model reaction.

Fig. 12 FT-IR spectra of the (a) Ni−Arg@ZY before the reaction and (b) after five cycles.

3.1.6. X-ray diffraction (XRD) analysis of the Ni/Arg@ZY nanocomposite. Fig. 10 presents the X-ray diffraction pattern of the nanocatalyst (shown in purple, Ni/Arg@ZY), which closely resembles the XRD pattern of the original zeolite sample (green plot) and the reference (JCPDS no. 39-1380). As observed, by modifying previous methods, including the use of centrifugation and placing the sample in an ultrasonic bath, the crystallographic pattern and characteristic features of the zeolites were obtained in the XRD analysis. Due to the low concentration of nickel ions (Ni^{2+}), the characteristics of the nickel nanoparticles were not observed in the overall spectrum. By applying the Scherrer equation for the nanocatalyst, the nanoparticle size was found to be 25.48 nm. As observed in the particle size distribution histogram obtained from the FESEM image, the majority of particles fall within the range of 25 to 30 nm, which shows a very good agreement with the X-ray diffraction (XRD) results and collectively confirms the nanostructure of the synthesized catalyst. Finally, to determine the extent of nickel

exchange with sodium, atomic absorption analysis was performed, and the results indicate that approximately 18 wt% of nickel was successfully anchored on the zeolite support.

After a comprehensive discussion on the design, synthesis, and characterization of Ni/Arg@zeolite-Y nanoparticles, we will now focus on examining their activity and performance in the synthesis of thieno[2,3-*d*]pyrimidinone derivatives.

3.2. Evaluation of the catalytic activity of Ni/Arg@zeolite-Y to synthesize thieno[2,3-*d*]pyrimidinone derivatives

In the first step of this study, 2-amino-4,5,6,7-tetrahydrobenzo [*b*]thiophene-3-carboxamide (**1**) was synthesized following the synthetic route outlined in Scheme 3. Its structure was confirmed by comparing its properties with those of the compounds reported in the scientific literature.[33]

In the next step, the reaction between **1** and benzaldehyde, catalyzed by Ni−Arg@ZY (10% wt/wt), was selected as a model reaction and conducted in ethanol solvent at 80 °C. After evaluating the feasibility of the reaction and product formation in the presence of the catalyst, optimization studies were carried out by varying the solvent types and catalyst loadings. The results are summarized in Table 2. According to Table 2, the highest product yield was obtained with 6% catalyst loading, using ethanol as the solvent, at 80 °C, and after 15 minutes (Table 2, entry 4).

After optimizing the reaction conditions for the model reaction, the method was further expanded by performing a one-pot reaction between 2-amino-4,5,6,7-tetrahydrobenzo[*b*] thiophene-3-carboxamide (**1**) and various aryl aldehydes (**2a– m**), bearing electron-withdrawing and electron-donating substituents. The corresponding thieno[2,3-*d*]pyrimidinone derivatives (**3a–m**) were synthesized with satisfactory yields, and the results are presented in Table 3.

After optimizing the conditions for the model reaction, the reusability of the Ni−Arg@ZY nanocatalyst was investigated. Upon completion of the reaction, the Ni−Arg@ZY nanocatalyst was easily separated from the reaction mixture using filtration. It was then washed several times with ethanol and dried in
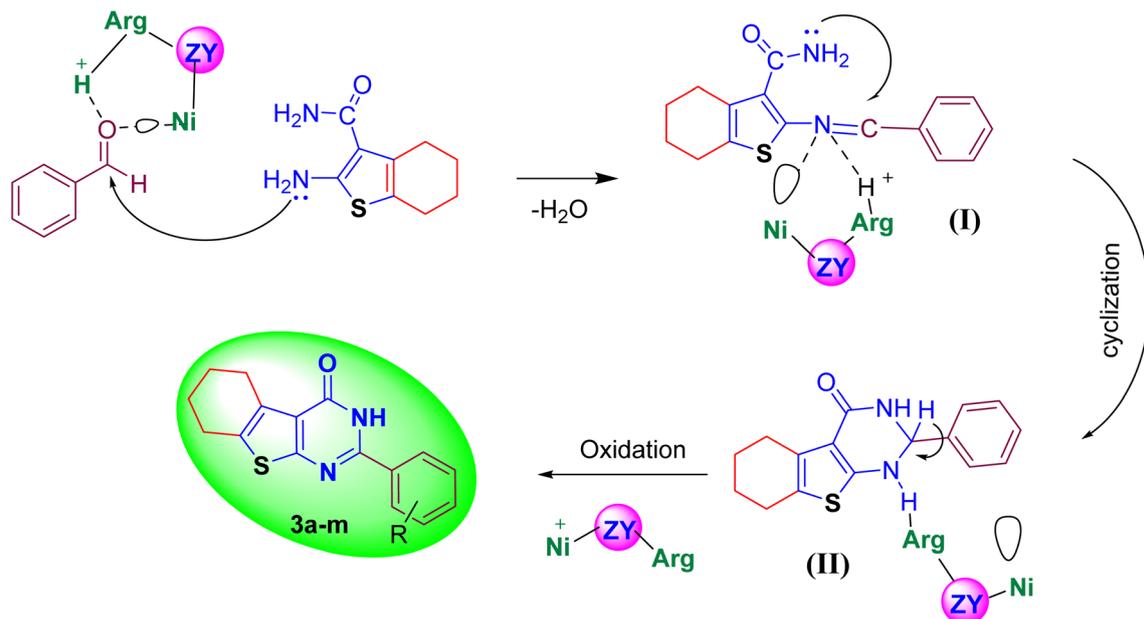
Scheme 4 The proposed mechanism for the preparation of thieno[2,3-*d*]pyrimidinones using Ni–Arg@ZY catalyst.

Table 4 Comparison of the synthesis of thienopyrimidinone (**3a**) using the Ni–Arg@ZY catalyst with other reported methods

Entry	Catalyst	Conditions	Time (min)	Yield (%)
1	Piperidine (1.5 mL)	DMF, reflux	30	65 (ref. 35)
2	HCl (0.1 mL)	*n*-BuOH, 80 °C	720	74 (ref. 33)
3	CeO$_2$–MgO (0.025 g)	Free solvent, 140 °C	90	90 (ref. 37)
4	Glacial acetic acid	DMSO, reflux	120	96 (ref. 31)
5	Ni–Arg@ZY (0.006 g)	EtOH, 80 °C	15	90 (this work)

a vacuum oven. The nanocatalyst could be reused up to five times without significant loss of activity. The results of the reusability of the Ni–Arg@ZY nanocatalyst are shown in Fig. 11.

To confirm this, the FT-IR spectra of the Ni–Arg@ZY nanocatalyst before the reaction and after five cycles of reuse are presented in Fig. 12. Based on the findings from this study, as discussed in previous sections, it appears that the use of 6 mg of Ni–Arg@ZY nanocatalyst in the synthesis of thieno[2,3-*d*] pyrimidinone derivatives (**3a–m**) *via* the reaction between 2-amino-4,5,6,7-tetrahydrobenzo[*b*]thiophene-3-carboxamide (**1**, 1 mmol) and aromatic aldehydes (**2a–m**) in ethanol under reflux conditions is an efficient and effective method.

In Scheme 4, the outlined mechanism for synthesizing 2-aryl thienopyrimidines is depicted. Initially, the carbonyl aldehyde group is activated either through the Lewis acid sites of nickel ions or the Brønsted acid of the amino acid's organic group on the zeolite support. Subsequently, the amine in compound (**1**) carries out a nucleophilic attack on the aldehyde's electrophilic center, leading to the elimination of a water molecule and forming the imine intermediate (**I**). Schiff base (**I**) can then be isolated from the reaction vessel. The imine group is further activated by the nanocatalyst, prompting a nucleophilic attack by the amide group, which induces cyclization and formation of the pyrimidine ring, yielding intermediate (**II**). Ultimately,

catalytic oxidation of this intermediate produces the final product **3a–m**. To validate the pathway of proposed mechanism, the Schiff base intermediate (**I**) associated with compound **3a** was successfully isolated from the reaction medium after 4 minutes. The structure of the intermediate was unequivocally characterized and confirmed by ^{1}H and ^{13}C NMR spectroscopic analyses (SI, Fig. S21 and S22).

Subsequently, a comparison is made between the optimized conditions obtained in this study for the synthesis of thieno[2,3-*d*]pyrimidinone derivatives and those reported in previous studies, as shown in Table 4. The table summarizes the various reaction conditions, including catalyst type, solvent, temperature, and reaction time, employed in earlier works. The results clearly highlight the efficiency and advantages of the method developed in this study, emphasizing its superior performance in terms of reaction yield, selectivity, and other milder conditions compared to previously reported methods.

4. Conclusion

In this study, the zeolite structure was first modified by incorporating nickel ions and L-arginine amino acid to form the Ni/Arg@zeolite-Y nanocomposite. The structural characteristics of the synthesized multi-functional catalyst was identified and

characterized using various techniques. Subsequently, the catalytic performance of the prepared nanomaterial was evaluated by employing it in the one-pot synthesis of thieno[2,3-*d*] pyrimidinone derivatives. Notably, the advantages of this reaction include high yield, short reaction time, the use of a non-toxic solvent, ease of product isolation, and the design and application of a heterogeneous, bioorgano-metallic, recyclable, and environmentally friendly nanocatalyst.

Author contributions

Conceptualization, supervision, review, figure creation, interpretation of nanocatalyst identification analyses, and final editing of the manuscript [Mehdi Kalhor]. Fabrication of the nanocatalyst, experimental work, and synthesis of the target heterocyclic compounds [Ziba Modares]. Manuscript writing, review, editing and verification of results [Vahid Azizkhani]. All authors have read and approved the final manuscript.

Conflicts of interest

The authors declare that they have no interest to influence the work reported in this paper.

Data availability

All datasets generated for this study are available in the manuscript and/or SI.

The original structural identification spectra of the products are available in the SI. See DOI: https://doi.org/10.1039/d5ra04062k.

Acknowledgements

References

1 N. O. Solomon, P. Simpa, O. A. Adenekan and S. C. Obasi, Sustainable nanomaterials' role in green supply chains and environmental sustainability, *Eng. Sci. Technol. J.*, 2024, **5**, 1678–1694.

2 F. Sher, I. Ziani, M. Hameed, S. Ali and J. Sulejmanović, Advanced nanomaterials design and synthesis for accelerating sustainable biofuels production – A review, *Curr. Opin. Green Sustainable Chem.*, 2024, **47**, 100925.

3 Ü. Y. Yıldız, R. Keçili and C. M. Hussain, Green and sustainable chemistry, *Green Imprinted Materials*, Elsevier, 2024, ch. 1, pp. 3–25.

4 R. O. Afolabi, A comprehensive review of nanosystems' multifaceted applications in catalysis, energy, and the environment, *J. Mol. Liq.*, 2024, **397**, 124190.

5 I. Ahmad, M. A. Aftab, A. Fatima, S. D. Mekkey, S. Melhi and S. Ikram, A comprehensive review on the advancement of transition metals incorporated on functional magnetic nanocomposites for the catalytic reduction and photocatalytic degradation of organic pollutants, *Coord. Chem. Rev.*, 2024, **514**, 215904.

6 D. N. Gaikwad, S. T. Gaikwad, R. K. Manjul, A. S. Rajbhoj, D. M. Suryavanshi, G. A. Varade and N. S. Dhane, A Comprehensive Overview of Recent Trends in the Production of Nitrogen-Containing Heterocyclic Compounds Using Nanocatalysts, *Lett. Org. Chem.*, 2025, **22**, 102–115.

7 M. R. Das, N. Hussain, R. Duarah, N. Sharma, P. Sarmah, A. Thakur, P. Bhattacharjee, U. Bora and R. Boukherroub, Metal Nanoparticles Decorated Two-Dimensional Nanosheets as Heterogeneous Catalysts for Coupling Reactions, *Catal. Rev.: Sci. Eng.*, 2022, **66**, 923–995.

8 D. Jagadeesan, Multifunctional nanocatalysts for tandem reactions: A leap toward sustainability, *Appl. Catal., A*, 2016, **511**, 59–77.

9 C. Srilakshmi and R. Saraf, Structural studies of multifunctional $SrTiO_3$ nanocatalyst synthesized by microwave and oxalate methods: Its catalytic application for condensation, hydrogenation, and amination reactions, *ACS Omega*, 2018, **3**, 10503–10512.

10 M. Kalhor, Z. Orouji and M. Khalaj, 4-Methylpyridinium chloride ionic liquid grafted on Mn@zeolite-Y: Design, fabrication and performance as a novel multi-functional nanocatalyst in the four-component synthesis of pyrazolophthalazine-diones, *Microporous Mesoporous Mater.*, 2022, **329**, 111498.

11 M. Kalhor, Z. Vahedi and H. Gharoubi, Design of a new method for one-pot synthesis of 2-amino thiazoles using trichloroisocyanuric acid in the presence of a novel multi-functional and magnetically catalytic nanosystem: Ca/4-MePy-IL@ZY-Fe_3O_4, *RSC Adv.*, 2023, **13**, 9208–9221.

12 Y. Wang, X. Ma, H. Wang, D. Zhao, Y. Liu and Z. Ma, Enhancement of Gaseous o-Xylene Elimination by Chlorosulfonic Acid-Modified H-Zeolite Socony Mobil-5, *Molecules*, 2024, **29**, 3507.

13 N. Salleh, M. M. Mahat, S. M. Yahaya and R. Ramli, Kinetic and Mechanism of Zerumbone Release from Cross-Linked Gelatin-Zeolite Y Hybrid for Oral Anticancer Drug Delivery, *J. Adv. Res. Micro Nano Eng.*, 2024, **18**, 32–43.

14 M. Al-Samhan and J. Al-Fadhli, Synthesis and Assessment of Y-Zeolite Catalyst for Direct Olefin Production from Heavy Feedstock: An Effect of Feed Composition, *Catal. Lett.*, 2024, **154**, 4719–4728.

15 B. Muir and T. Bajda, Organically modified zeolites in petroleum compounds spill cleanup – Production, efficiency, utilization, *Fuel Process. Technol.*, 2016, **149**, 153–162.

16 B. Muir, M. Wołowiec, T. Bajda, P. Nowak and P. Czupryński, The Removal of Organic Compounds by Natural and Synthetic Surface-Functionalized Zeolites: A Mini-Review, *Period. Mineral.*, 2017, **48**, 145–156.

17 M. Tomašević-Čanović, A. Daković, G. Rottinghaus, S. Matijašević and M. Đuričić, Surfactant modified zeolites new efficient adsorbents for mycotoxins, *Microporous Mesoporous Mater.*, 2003, **61**, 173–180.

18 A. Ehsani, M. K. Moftakhar and M. Kalhor, Mesoporous ionic liquid functionalized nanozeolite: Synthesis and high efficient material to improving pseudocapacitance performance of conductive polymer, *J. Energy Storage*, 2022, **55**, 105489.

19 J. Paradowska, M. Stodulski and J. Mlynarski, Catalysts Based on Amino Acids for Asymmetric Reactions in Water, *Angew. Chem., Int. Ed.*, 2009, **48**, 4288–4297.

20 L.-W. Xu and Y. Lu, Primary amino acids: privileged catalysts in enantioselective organocatalysis, *Org. Biomol. Chem.*, 2008, **6**, 2047–2053.

21 S. Malhotra, D. Jaspal and A. Malviya, Amino acids as catalysts for the enolisation study of *m*-Methylacetophenone, *Arabian J. Chem.*, 2019, **12**, 1247–1251.

22 K. Kamanna, Organocatalysts based on natural and modified amino acids for asymmetric reactions, *Phys. Sci. Rev.*, 2022, **7**, 429–467.

23 F. Bijari, M. Talebi, H. Ghafuri, Z. Tajik and P. Hanifehnejad, Graphitic Carbon Nitride-Supported L-Arginine: Synthesis, Characterization, and Catalytic Activity in Multi-Component Reactions, *Chem. Proc.*, 2022, **12**, 50.

24 G. Fu, Q. Zhang, J. Wu, D. Sun, L. Xu, Y. Tang and Y. Chen, Arginine-mediated synthesis of cube-like platinum nanoassemblies as efficient electrocatalysts, *Nano Res.*, 2015, **8**, 3963–3971.

25 K. Azizi, M. Karimi, H. R. Shaterian and A. Heydari, Ultrasound irradiation for the green synthesis of chromenes using L-arginine-functionalized magnetic nanoparticles as a recyclable organocatalyst, *RSC Adv.*, 2014, **4**, 42220–42225.

26 H. S. Ali and S. P. de Visser, Catalytic divergencies in the mechanism of L-arginine hydroxylating nonheme iron enzymes, *Front. Chem.*, 2024, **12**, 1–14.

27 C. Wu, L. Zhang, Z. Zhou, L. Tan, Z. Wang, C. Guo and Y. Wang, Discovery and mechanistic insights into thieno [3,2-*d*]pyrimidine and heterocyclic fused pyrimidines inhibitors targeting tubulin for cancer therapy, *Eur. J. Med. Chem.*, 2024, **276**, 116649.

28 H. K. A. El-Mawgoud, A. M. AboulMagd, M. T. M. Nemr, M. M. Hemdan, A. I. Hassaballah and P. S. Farag, Design, synthesis and cytotoxic evaluation of new thieno[2,3-*d*] pyrimidine analogues as VEGFR-2/AKT dual inhibitors, apoptosis and autophagy inducers, *Bioorg. Chem.*, 2024, **150**, 107622.

29 T. Manna, S. Maji, M. Maity, B. Debnath, S. Panda, S. A. Khan, R. Nath and M. J. Akhtar, Anticancer potential and structure activity studies of purine and pyrimidine derivatives: an updated review, *Mol. Diversity*, 2025, **29**, 817–848.

30 P. Lagardère, C. Fersing, N. Masurier and V. Lisowski, Thienopyrimidine: A Promising Scaffold to Access Anti-Infective Agents, *Pharmaceuticals*, 2022, **15**, 35.

31 A. Chiriapkin, I. Kodonidi and D. Pozdnyakov, Targeted Synthesis and Study of Anti-tyrosinase Activity of 2-Substituted Tetrahydrobenzo[4,5]Thieno[2,3-*d*]Pyrimidine-4(3H)-One, *Iran. J. Pharm. Res.*, 2022, **21**, e126557.

32 M. T. M. Sayed, R. A. Hassan, P. A. Halim and A. K. El-Ansary, Recent updates on thienopyrimidine derivatives as anticancer agents, *Med. Chem. Res.*, 2023, **32**, 659–681.

33 H. Amawi, C. Karthikeyan, R. Pathak, N. Hussein, R. Christman, R. Robey, C. R. Ashby Jr., P. Trivedi, A. Malhotra and A. K. Tiwari, Thienopyrimidine derivatives exert their anticancer efficacy via apoptosis induction, oxidative stress and mitotic catastrophe, *Eur. J. Med. Chem.*, 2017, **138**, 1053–1065.

34 I. Soerjomataram and F. Bray, Planning for tomorrow: global cancer incidence and the role of prevention 2020–2070, *Nat. Rev. Clin. Oncol.*, 2021, **18**, 663–672.

35 S. G. Dzhavakhishvili, N. Yu. Gorobets, B. V. Paponov, V. I. Musatov and S. M. Desenko, Three Possible Products from the Reactions of Gewald's Amide with Aromatic Aldehydes, *J. Heterocycl. Chem.*, 2008, **45**, 573–577.

36 Y. D. Wang, S. Johnson, D. Powell, J. P. McGinnis, M. Miranda and S. K. Rabindran, Inhibition of tumor cell proliferation by thieno[2,3-*d*]pyrimidin-4(1H)-one-based analogs, *Bioorg. Med. Chem. Lett.*, 2005, **15**, 3763–3766.

37 F. Ghayour, M. R. Mohammad Shafiee and M. Ghashang, ZnO-CeO$_2$ nanocomposite: efficient catalyst for the preparation of thieno[2,3-*d*]pyrimidin-4(3H)-one derivatives, *Main Group Met. Chem.*, 2018, **41**, 21–26.

38 F. M. Elmenier, D. S. Lasheen and K. A. M. Abouzid, Design, synthesis, and biological evaluation of new thieno[2,3-*d*] pyrimidine derivatives as targeted therapy for PI3K with molecular modelling study, *J. Enzyme Inhib. Med. Chem.*, 2022, **37**, 315–332.

39 H. Mehrabi, F. Alizadeh-Bami and S. Alinaghi-Langari, Microwave-Assisted Synthesis of 2-Aryl-5,6,7,8-tetrahydrobenzo[4,5]thieno[2,3-*d*]pyrimidinones, *ChemistrySelect*, 2024, **9**, e202404000.

40 L. D. Jennings, S. L. Kincaid, Y. D. Wang, G. Krishnamurthy, C. F. Beyer, J. P. McGinnis, M. Miranda, C. M. Discafani and S. K. Rabindran, Parallel synthesis and biological evaluation of 5,6,7,8-tetrahydrobenzothieno[2,3-d]pyrimidin-4(3H)-one cytotoxic agents selective for p21-deficient cells, *Bioorg. Med. Chem. Lett.*, 2005, **15**, 4731–4735.

41 A. Mavrova, S. Dimov, D. Vuchev, K. Anichina and D. Yancheva, Antihelminthic Activity of Some 2-Substituted Thieno[2,3-d]pyrimidin-4-ones, *Lett. Drug Des. Discovery*, 2018, **15**, 887–894.

42 M. Kalhor, M. Bigdeli and H. Moghanian, Ni@zeolite-Fe$_3$O$_4$ supported 4-methylpyridinium ionic liquid: design and application as a new multi-functional and magnetically catalytic nanosystem in three-component synthesis of 4-aryl oxazolones, *Res. Chem. Intermed.*, 2023, **49**, 5375–5394.

43 M. Kalhor, S. Banibairami and S. A. Mirshokraie, Ni@zeolite-Y nanoporous; a valuable and efficient nanocatalyst for the synthesis of *N*-benzimidazole-1,3-thiazolidinones, *Green Chem. Lett. Rev.*, 2018, **11**, 334–344.

44 M. Kalhor and Z. Zarnegar, Fe$_3$O$_4$/SO$_3$H@zeolite-Y as a novel multi-functional and magnetic nanocatalyst for clean and soft synthesis of imidazole and perimidine derivatives, *RSC Adv.*, 2019, **9**, 19333–19346.

45 M. Kalhor and S. Banibairami, Design of a new multi-functional catalytic system Ni/SO$_3$H@zeolite-Y for three-component synthesis of *N*-benzo-imidazo- or -thiazole-1,3-thiazolidinones, *RSC Adv.*, 2020, **10**, 41410–41423.

46 C. Yang and Q. Xu, Aluminated Zeolites β and Their Properties Part 1. Alumination of Zeolites β, *J. Chem. Soc., Faraday Trans.*, 1997, **93**, 1675–1680.

47 J. Perez-Pariente, J. A. Martens and P. A. Jacobs, Crystallization Mechanism of Zeolite Beta from (TEA)$_2$O, Na$_2$O and K$_2$O Containing Aluminosilicate Gels, *Appl. Catal.*, 1987, **31**, 35–64.

48 P. Li, Y. Wang, H. Li and G. Calzaferri, Luminescence enhancement after adding stoppers to europium(III) nanozeolite L, *Angew. Chem., Int. Ed.*, 2014, **53**, 2904–2909.